Theory of biexcitons in one-dimensional polymers

Frank B. Gallagher and Frank C. Spano
Department of Chemistry, Temple University, Philadelphia, Pennsylvania 19122
(Received 14 August 1995)

We calculate the biexciton phase space for a model polymer consisting of a one-dimensional array of N coupled quantum cells, each containing two levels. The Hamiltonian allows for electron and hole transfer (t) and includes on-site (V_0) and extended (V_1/r) Coulombic interactions. The double electron-hole pair basis set is numerically diagonalized for as many as $N=31$ cells. A phase boundary for two-photon-allowed biexcitons with A^+ symmetry is calculated in (α,β) space where $\alpha \equiv V_1/V_0$ and $\beta \equiv t/V_0$. The phase space generally supports multiple biexcitons; the most tightly bound biexciton exists over a region limited by $\beta \lesssim 0.11$ and $0.84 \lesssim \alpha \leqslant 1$. Higher-energy biexcitons occupy successively smaller corners of phase space centered on $\beta=0$ and $\alpha=1$. The two-photon absorption spectrum in the region $2\hbar\omega < 2\Delta$, where Δ is the one-photon gap, generally shows two types of peaks: high-energy ones associated with biexcitons and lower-energy peaks associated with single excitons of A^+ symmetry.

I. INTRODUCTION

The existence of biexcitons and their influence on the nonlinear optical response of conjugated polymers are currently subjects of considerable interest. Biexcitons are suspected in the two-photon absorption (TPA) spectra and pump-probe transient absorption spectra of several polymers including polydiacetylene (PDA),[1] polyparaphenylenevinylene (PPV),[2] and polysilane (PS).[3–6] Recently they have been discovered in the quasi-one-dimensional mixed organic charge-transfer crystal, Antracene/PMDA (Ref. 7) through high-intensity differential pump-probe spectroscopy. In conventional inorganic semiconductors biexcitons are well established,[8] being first observed in bulk CuCl almost three decades ago.[9]

The most popular theoretical treatment of the optical response in conjugated polymers is based on the Pariser-Parr-Pople (PPP) Hamiltonian in a basis set containing a single p_z orbital per carbon atom or two sp^3 orbitals per Si atom in the case of polysilanes.[10–12,14–18] Electron transfer is regulated by the near-neighbor coupling integrals $t(1\pm\delta)$, where δ is the alternation parameter, and Coulombic interactions are accounted for using the Ohno potential. Exact calculations by Soos and co-workers[10–12] can handle as many as $N=14$ orbitals, which for large alternation ($\delta > 0.6$) is sufficient to obtain accurate extrapolations to the polymer or long chain regime.[11] They also established that for intermediate alternations ($\delta \sim 0.33$) that pertain to polysilanes, for example, the lowest one- and two-photon allowed states have strong excitonic character.[12] Several other groups have developed exciton models, under which optical properties are attributed to one-dimensional (1D) Wannier excitons.[13–18,21] Abe has shown that the lowest one-photon allowed exciton consumes most of the oscillator strength in one dimension,[13] and has used only the lowest-energy one-exciton states to calculate the third-order nonlinear optical response.[14] The method is highly successful in describing TPA (Ref. 19) and third-harmonic generation from polysilanes[20] in the spectral region between 2 and 5 eV, but fails at higher energies where two-photon transitions to states with two e-h pairs appear.[3–6]

It is a formidable theoretical challenge to calculate the nonlinear optical response of a long-chain polymer in a way that handles the enormous double e-h pair basis set in a size consistent manner. Approaches based on singles and doubles configuration interaction[15] can treat as many as 40 orbitals, but suffer from being size inconsistent. Mukamel and Wang[16] developed an equations of motion theory that can treat several hundred orbitals but factorized the two-exciton correlation function. Our motivation for the present work was to develop a theory for nonlinear susceptibilities in conjugated polymers that includes charge transfer and Coulombic interactions in a size consistent way, allowing investigation of the large size or polymer limit. To this end we chose the one-dimensional version of the usual tight-binding two-band semiconductor Hamiltonian $\hat{H}_{e\text{-}h}$ written in an electron-hole representation. We consider a one-dimensional array of N quantum cells, each containing two levels. $\hat{H}_{e\text{-}h}$ includes the opposing forces of charge delocalization (t), and localization through on-site (V_0) and extended (V_1/r) Coulomb interactions. Previously,[21] we calculated the nonresonant third-order susceptibility, $\chi^{(3)}$, for this Hamiltonian but avoided the biexciton regime, which is the central focus of the current paper. The Hamiltonian is identical to that studied by Ostreich and Schonhammer[22] in their analysis of the Stark effect in 1D semiconductors and is similar to that used by Ishida[23] in his analysis of biexciton effects and lattice relaxation on the transient absorption spectrum of 1D polymers. A 3D version was analyzed by Ivanov and Haug[24] in order to describe two-photon absorption of biexcitons in direct-gap semiconductors such as CuCl.

Unlike the PPP Hamiltonian $\hat{H}_{e\text{-}h}$ commutes with the total number of electrons or holes. Thus there is no mixing between the one- and two-electron excitations, an effect that is important in weakly alternating polymers,[10–12] but much less so in polysilanes, for example. In polysilanes, the larger alternation causes the lowest-energy one-photon allowed state ($1B_u$) to be significantly lower in energy than the two-

photon allowed $2A_g$ state,[12] an ordering that is supported by experiment,[3–6] and that is preserved under $\hat{H}_{e\text{-}h}$. With the electron (or hole) number being a good quantum number comes the unambiguous definition of a biexciton, as any state with two e-h pairs that is lower in energy than twice the lowest one-exciton energy. Recently, Guo, Chandross, and Mazumdar[18] have proposed a definition of biexcitons under the PPP Hamiltonian based on energy and transition dipole moment (from the $1B_u$ state) considerations. Another advantage of our approach is that size consistency follows naturally and it is computationally far less intensive to calculate nonlinear optical properties.

Calculations of TPA are restricted to the case when the ground state is the one with no electrons or holes, G_0. Section III derives the conditions under which the ground state is G_0, as opposed to a charge density wave (CDW). The following section deals with one and two e-h excitations. When reflection, charge conjugation, and rotational symmetries are used to block diagonalize the Hamiltonian, we are able calculate one and two e-h pair eigenstates and eigenvalues for as many as 31 two-level quantum cells given the constraints of computer memory. We also develop a further approximation for small values of t/V_0 that truncates the electron-hole separation to at most one lattice spacing. This allows treatment of much larger sizes, on the order of several hundred cells. All of our calculations are conducted in the polymer limit, obtained by taking N sufficiently large to observe convergence. A demonstration of the consistency of the energy based definition of biexcitions with hole-hole localization is made in Sec. V. This is followed by a derivation of a biexciton phase space diagram in the dimensionless variables $\alpha=V_1/V_0$ and $\beta=t/V_0$. We find that the most tightly bound biexciton exists for small β ($\beta<0.11$) and α in the range $1\geqslant\alpha\gtrsim0.845$. There are also smaller regions containing multiple biexcitons centered about the point $\beta=0$ and $\alpha=1$.

In Sec. VI we calculate TPA in the model polymer for the case where the ground state, G_0 is a state with no electrons or holes, being careful to avoid parameter ranges that favor the CDW ground state. The spectral range is restricted so that the fundamental photon frequency is less than the lowest-energy $1B^-$ exciton transition frequency in order to avoid divergences from one-photon absorption. This is also the range over which most experiments are performed. We anticipate TPA peaks arising from two-photon allowed one excitons as well as biexcitons and work out the conditions under which the various peaks will be present. Several TPA spectra are calculated covering horizontal and vertical cuts through the biexciton phase space. We also study the behavior of the biexciton transition dipole moment from the $1B^-$ one-exciton state and compare it to recent predictions.[18] Section VII summarizes the main results and discusses applications to experiment.

II. HAMILTONIAN

The model polymer consists of N coupled quantum cells, where N is taken to be odd. In order to exploit periodic boundary conditions, the cell positions are taken to be at each of the vertices of a regular polygon with N sides of length a. With $a/2\sin(\pi/N)$ the radius of the circumscribed

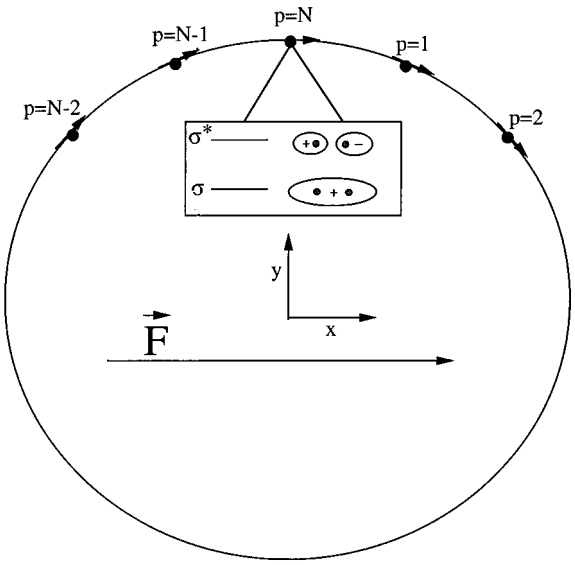

FIG. 1. Schematic representation of the model polymer. There are N unit cells, each containing two molecular orbitals and two electrons in the neutral case. The position of the pth cell is given by Eq. (1). Arrows indicate direction of the negative lobe of the antibonding orbital. Note that upon reflection through the yz plane the antibonding orbitals change sign but not the bonding ones.

circle, the position of the pth cell is

$$\mathbf{r}_p=\frac{a}{2\sin(\pi/N)}\{\sin(2\pi p/N)\hat{i}+\cos(2\pi p/N)\hat{j}\}, \quad (1)$$

where $\hat{i}$ and $\hat{j}$ are unit vectors along the x and y axes, respectively. Figure 1 shows the schematic of the model. In this work we are not concerned with finite-size effects. The polymer limit corresponds to taking N large enough (with the nearest-neighbor distance a held constant) to observe convergence in the quantities of interest.

Each quantum cell contains two levels, corresponding to two Wannier functions, for example, denoted as σ (ground) and σ^* (excited). σ is symmetric, while σ^* is antisymmetric with respect to a local inversion center on the polymer backbone. The two levels are connected via a transition dipole moment $\boldsymbol{\mu}_c$, taken to lie along the polymer backbone (see Fig. 1). This arrangement corresponds to an idealized polysilane chain, for example, where each cell consists of two Si atoms, with in- and out-of-phase combinations of the two overlapping silicon sp^3 orbitals forming the bonding (σ) and antibonding (σ^*) molecular orbitals. A charge neutral cell contains two electrons; the ground-state configuration is σ^2, while the optically driven excited state or bond exciton is $\sigma^1\sigma^{*1}$. The bond exciton may ionize into a charge separated species consisting of a monovalent anion ($\sigma^2\sigma^{*1}$) and a monovalent cation (σ^1). All other configurations, such as doubly ionized states, are discounted.

In an electron-hole representation, the two-band Hamiltonian that describes the array of coupled quantum cells is given by

$$\hat{H}_{e\text{-}h}=\sum_{p=1}^{N}(e_e\hat{c}_p^{\dagger}\hat{c}_p+e_h\hat{d}_p^{\dagger}\hat{d}_p)-\sum_{p=1}^{N}\{t_e(\hat{c}_p^{\dagger}\hat{c}_{p+1}+\hat{c}_{p+1}^{\dagger}\hat{c}_p)+t_h(\hat{d}_p^{\dagger}\hat{d}_{p+1}+\hat{d}_{p+1}^{\dagger}\hat{d}_p)\}+\frac{1}{2}\sum_{pp'}V(p-p')\{\hat{c}_p^{\dagger}\hat{c}_{p'}^{\dagger},\hat{c}_{p'},\hat{c}_p$$
$$+\hat{d}_p^{\dagger}\hat{d}_{p'}^{\dagger},\hat{d}_{p'},\hat{d}_p-2\hat{c}_p^{\dagger}\hat{d}_{p'}^{\dagger},\hat{d}_{p'},\hat{c}_p\},\tag{2}$$

where $\hat{c}_p^{\dagger}$ ($\hat{d}_p^{\dagger}$) creates an electron (hole) in σ^* (σ) at the pth cell and periodic boundary conditions are imposed. All operators obey Fermi commutation relations. In Eq. (2) a constant representing the energy of the filled valence band is omitted; hence the ground state G_0 with no electrons or holes has zero energy. The first two sums include the effective one-particle energies of the electrons and holes. e_e+e_h is the single cell transition energy omitting the electron-hole interaction but including the average interaction between the electron and hole with the filled valence band. The electron (hole) transfer integral is $-t_e$ ($-t_h$), with t_e,t_h taken positive, as for a direct-gap semiconductor. The pairwise Coulombic potential $V(p-p')$ is

$$V(p-p')=V_0,\quad p=p'\tag{3a}$$

$$V(p-p')=V_1/|p-p'|,\quad 0<|p-p'|\leqslant(N-1)/2,\tag{3b}$$

with $V_0,V_1>0$. For $(N-1)/2<|p-p'|\leqslant N-1$, $V(p-p')$ is obtained by replacing $|p-p'|$ with $N-|p-p'|$ in Eq. (3b). The extended interaction in (3b) assumes a distance $|p-p'|a$ between cells p and p' and not the length of the connecting chord, which is correct for a finite ring. In the polymer limit the use of Eq. (3b) is exact. The final sum in Eq. (2) represents the electron and hole interactions, which may ultimately lead to excitons and biexcitons.

Because the Hamiltonian in Eq. (2) commutes with the total number of electrons, it can be decomposed into diagonal blocks, $\hat{H}_n$, each with n electrons and n holes in the case of the neutral chain considered here. Invoking charge conjugation symmetry allows further block diagonalization, making possible investigations for larger N. We therefore set $t\equiv t_e=t_h$ and obtain

$$\hat{H}_1=(e_e+e_h)/V_0-\beta\sum_{p=1}^{N}(\hat{c}_p^{\dagger}\hat{c}_{p+1}+\hat{c}_{p+1}^{\dagger}\hat{c}_p+\hat{d}_p^{\dagger}\hat{d}_{p+1}+\hat{d}_{p+1}^{\dagger}\hat{d}_p)-\sum_{pp'}\alpha(p-p')\hat{c}_p^{\dagger}\hat{d}_{p'}^{\dagger},\hat{d}_{p'},\hat{c}_p,\tag{4a}$$

$$\hat{H}_2=2(e_e+e_h)/V_0-\beta\sum_{p=1}^{N}(\hat{c}_p^{\dagger}\hat{c}_{p+1}+\hat{c}_{p+1}^{\dagger}\hat{c}_p+\hat{d}_p^{\dagger}\hat{d}_{p+1}+\hat{d}_{p+1}^{\dagger}\hat{d}_p)+\frac{1}{2}\sum_{pp'}\alpha(p-p')\{\hat{c}_p^{\dagger}\hat{c}_{p'}^{\dagger},\hat{c}_{p'},\hat{c}_p+\hat{d}_p^{\dagger}\hat{d}_{p'}^{\dagger},\hat{d}_{p'},\hat{d}_p$$
$$-2\hat{c}_p^{\dagger}\hat{d}_{p'}^{\dagger},\hat{d}_{p'},\hat{c}_p\},\tag{4b}$$

where the Hamiltonians have been made dimensionless through division by the on-site potential V_0. The dimensionless electron or hole transfer term is

$$\beta\equiv t/V_0,\tag{5}$$

and the dimensionless Coulombic interaction is

$$\alpha(p-p')\equiv V(p-p')/V_0,\tag{6}$$

so that $\alpha(0)=1$ and $\alpha(n)=\alpha/n$ ($n\geqslant 1$). The long-range Coulombic interaction is therefore characterized by a single parameter,

$$\alpha\equiv V_1/V_0.\tag{7}$$

In all that follows the values of α are limited to the range

$$0\leqslant\alpha\leqslant 1,\tag{8}$$

where the upper limit follows from $V_1\leqslant V_0$.

The one and two e-h pair eigenstates depend only on α and β, while the ith eigenvalue (energy) of $\hat{H}_n$, $E_i^{(n)}$, requires a third parameter, e_e+e_h. Taking advantage of the fact that the lowest eigenvalue of $\hat{H}_1$ corresponds to a one-photon allowed state (which is readily measured in a linear absorption experiment) we choose the third parameter to instead be Δ, the one-photon energy gap, defined as

$$\Delta\equiv e_e+e_h+V_0f_1^{(1)}(\alpha,\beta),\tag{9}$$

where $f_i^{(n)}(\alpha,\beta)$ are the eigenvalues of $[\hat{H}_n-n(e_e+e_h)/V_0]$, ordered so that $i=1$ is the lowest value. The dimensionless ith eigenvalue of $\hat{H}_n$, $E_i^{(n)}$ can then be written as

$$E_i^{(n)}=n\frac{\Delta}{V_0}+[f_i^{(n)}(\alpha,\beta)-nf_1^{(1)}(\alpha,\beta)],\tag{10}$$

from which it follows that $\Delta=V_0E_1^{(1)}$ by taking $n=i=1$.

We conclude this section with the Hamiltonian that describes the interaction of the polymer with light. For an electric field **F** oriented along the x axis the interaction is represented within the dipole approximation by $\hat{H}_{\rm int}=-\hat{\mu}_xF$, where $\hat{\mu}$ is the polymer transition dipole moment operator. The second quantized form of $\hat{\mu}_x$ is

$$\hat{\mu}_x=\mu_c\sum_{p=1}^{N}(c_p^{\dagger}d_p^{\dagger}+d_pc_p)+\frac{ea}{2\sin\pi/N}\sum_{p=1}^{N}\sin(2\pi p/N)$$
$$\times\{d_p^{\dagger}d_p-c_p^{\dagger}c_p\},\tag{11}$$

where Eq. (1) was used in the second term. The first term in Eq. (11) induces interband transitions between the ground state and the single e-h pair manifold, and between the single e-h pair manifold and the double e-h pair manifold.

Since we are ultimately concerned with linear polymers (and not rings) the first term neglects the change in the vector product $\boldsymbol{\mu}_c \cdot \hat{i}$ as the ring is traversed. This leads to the $\Delta k=0$ optical selection rule where k is the center-of-mass momentum of the multiparticle state. The second term in Eq. (11) represents the intercell transition dipole moment, and is responsible for intraband transitions that conserve the number of e-h pairs. Replacing the sines by their small argument approximations would yield the straight chain version but it would *not* be invariant to a rotation by N. This leads to large N divergences[17] in its matrix elements with the wave functions of H_1 or H_2 which *are* periodic in N. Hence the sine dependence must be retained.

III. GROUND STATE OF $\hat{H}_{e\text{-}h}$

Before focusing on the one and two e-h pair manifolds let us more carefully consider the ground state of the full Hamiltonian, $\hat{H}_{e\text{-}h}$. In the optical response section (VI) we consider only the case where the ground state is the state with no electrons or holes, denoted as G_0. However $\hat{H}_{e\text{-}h}$ also supports a CDW ground state. To see this consider first the case $\beta=0$. In a lattice containing N sites, a CDW consists of alternating array of $N/2$ electrons and $N/2$ holes. The energy of this state (in units of V_0) is given by

$$E_{\mathrm{CDW}}=\frac{N}{2}\left[\frac{\Delta}{V_0}+(1-2\ln 2\alpha)\right], \quad \beta=0, \tag{12}$$

where $2\ln 2$ is Madalung's constant in one dimension and $\Delta=e_e+e_h-V_0$ is the one-photon band gap for $\beta=0$. Maintaining $\Delta>0$, the energy of the CDW can fall below zero, displacing G_0 as the ground state whenever

$$\alpha>1/2\ \ln 2\approx 0.72. \tag{13}$$

Within this range of α, a CDW phase transition occurs at $E_{\mathrm{CDW}}=0$, or, from Eq. (12), when $\Delta/V_0=2\ln 2\alpha-1$. Hence, for $\beta=0$ the ground state is G_0 when

$$\frac{\Delta}{V_0}>2\alpha\ln 2-1; \tag{14}$$

otherwise the ground state is a CDW.

For small nonzero values of β (with $\beta^2\ll 1$) there is a negative second-order correction to the CDW energy, given by $-2N\beta^2/[(4\ln 2-1)\alpha-1]$, where $[(4\ln 2-1)\alpha-1]$ is the energy required to transfer a given charge (positive or negative) on the CDW to a neighboring site, creating a bond exciton and a neighboring cell in it ground state (σ^2). The energy of the charge density wave can then be written as

$$E_{\mathrm{CDW}}=\frac{N}{2}\left[\frac{\Delta}{V_0}-\left\{f_1^{(1)}(\alpha,\beta)+2\alpha\ln 2 + \frac{4\beta^2}{(4\ln 2-1)\alpha-1}\right\}\right], \quad \beta^2\ll 1, \tag{15}$$

where Eq. (9) was used for the one-photon gap, Δ. Taking $E_{\mathrm{CDW}}=0$, yields an equation in the three independent variables Δ/V_0, α, and β, which defines a phase boundary surface. In Fig. 2 we show the (α,β) dependence of the phase boundary for several values of Δ/V_0. The numerical analysis of Fig. 2 shows that the $\beta=0$ condition from Eq. (14) can be extended for *any* point (α,β): there are no CDW's as long as $\Delta/V_0>2\ln 2-1\approx 0.386$. As Δ/V_0 decreases below this value the CDW region occupies an increasing larger corner in phase space near $\alpha=1$ and $\beta=0$. The phase-space diagram in Fig. 2 is strictly valid for $\beta^2\ll 1$. This range of β is sufficient, however, to completely characterize biexcitons as is shown in Sec. V.

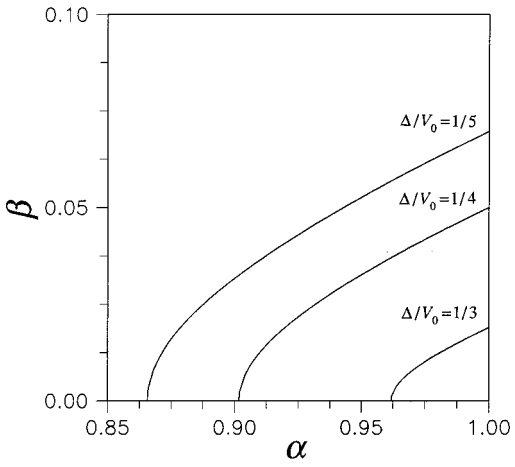

FIG. 2. Phase boundaries separating the neutral ground state G_0 containing no electrons or holes and the CDW ground state for several values of Δ/V_0. CDW ground states exists at all points under the curves.

IV. ONE- AND TWO-PHOTON ALLOWED EIGENSTATES

In labeling the excited states of the Hamiltonian it is convenient and customary to indicate the symmetries of the states with respect to reflection and inversion. In our case we consider a ring with an odd number of cells, which lacks an inversion center. However, the Hamiltonians in Eq. (4) are still invariant under reflection about the site $p=N$ (see Fig. 1) and under the interchange of electron and holes. Hence we adapt a notation that indicates the symmetries with respect to these two operations as well as the number of electron-hole pairs.

The reflection and exchange operations, denoted as $\hat{R}$ and $\hat{Q}$ respectively, are defined through their effects on the electron and hole creation and annihilation operators:

$$\hat{R}\begin{pmatrix} d_p \\ d_p^\dagger \end{pmatrix}=\begin{pmatrix} d_{N-p} \\ d_{N-p}^\dagger \end{pmatrix} \quad \text{and} \quad \hat{R}\begin{pmatrix} c_p \\ c_p^\dagger \end{pmatrix}=-\begin{pmatrix} c_{N-p} \\ c_{N-p}^\dagger \end{pmatrix} \tag{16a}$$

and

$$\hat{Q}\begin{pmatrix} c_n \\ c_n^\dagger \end{pmatrix}=\begin{pmatrix} d_n \\ d_n^\dagger \end{pmatrix} \quad \text{and} \quad \hat{Q}\begin{pmatrix} d_n \\ d_n^\dagger \end{pmatrix}=\begin{pmatrix} c_n \\ c_n^\dagger \end{pmatrix}. \tag{16b}$$

Because $\hat{Q}$ and $\hat{R}$ commute with $\hat{H}_n$ and $\hat{Q}^2=\hat{R}^2=1$, the eigenstates of $\hat{H}_n$ are simultaneously eigenstates of $\hat{R}$ and $\hat{Q}$ with eigenvalues of $+1$ (symmetric) or -1 (antisymmetric). The transition dipole moment operator in Eq. (11) is antisymmetric with respect to both operations,

$$\hat{R}\hat{\mu}_x = -\hat{\mu}_x, \tag{17a}$$

$$\hat{Q}\hat{\mu}_x = -\hat{\mu}_x. \tag{17b}$$

It then follows that starting from a ground state G_0 with the full symmetry of the Hamiltonian, only eigenstates that are antisymmetric with respect to both operations are one-photon allowed, while states that are symmetric with respect to both operations are two-photon allowed.

The mth one-photon allowed eigenstate of $\hat{H}_1$ with a single electron-hole pair is designated as $mB^-(1)$, where B^- denotes odd symmetry with respect to reflection (B) and charge conjugation ($-$). The number of electron-hole pairs is enclosed in the bracket. States are indexed according to their energy with $m=1$ corresponding to the state with lowest energy. Although not indicated in the label the one-photon allowed $mB^-(1)$ states are also invariant to ring rotations by $(2\pi/N)s$ radians $[s=\pm1,\pm2,\ldots,\pm(N-1)/2]$ and hence carry a center-of-mass momentum of zero. This follows from the $\Delta k=0$ selection rule embodied in the interband transition dipole moment in Eq. (11). Such $mB^-(1)$ states can be expanded as

$$mB^-(1)=\sum_{p=1}^{N}\sum_{n=-(N-1)/2}^{(N-1)/2} a_{k=0}^{(m)}(n)d_p^\dagger c_{p+n}^\dagger|G\rangle,$$

$$a_{k=0}^{(m)}(n)=a_{k=0}^{(m)}(-n), \tag{18}$$

where n designates the distance between the electron and hole and the k index in the expansion coefficients indicates a center-of-mass momentum of zero. The expansion coefficients are even with respect to electron-hole interchange, although the symmetry of the entire wave function is odd. (This follows because of the additional sign change induced by reordering of the electron and hole fermion operators.)

The mth two-photon allowed state with one electron-hole pair is designated as $mA^+(1)$, where A^+ denotes even symmetry with respect to reflection (A) and charge conjugation ($+$). Such states are optically allowed from the $mB^-(1)$ states and can be expanded as

$$mA^+(1)=\sum_{p=1}^{N}\sum_{n=-(N-1)/2}^{(N-1)/2}\cos\left[\frac{\pi}{N}(2p+n)\right]\times a_{k=2\pi/N}^{(m)}(n)d_p^\dagger c_{p+n}^\dagger|G\rangle,$$

$$a_{k=2\pi/N}^{(m)}(-n)=-a_{k=2\pi/N}^{(m)}(n). \tag{19}$$

These states carry a vanishingly small center-of-mass momentum of $\pm 2\pi/Na$, and result when the intraband transition dipole moment operator in Eq. (11) operates on $mB^-(1)$. Note that the expansion coefficients are now odd with respect to electron-hole interchange. Figure 3 shows an energy-level diagram including only the one- and two-photon allowed eigenstates of $\hat{H}_1$. $1B^-(1)$ is lowest in energy, followed by $1A^+(1)$ and $2B^-(1)$. Higher-energy states are not shown. The alternating order is characteristic of $\hat{H}_1$ in the polymer limit.

Finally, let us consider the two-photon allowed eigenstates of $\hat{H}_2$ having two electron-hole pairs. The total number of four-particle eigenstates is $N^2(N-1)^2/4$. If we include only those states with a center-of-mass momentum of zero

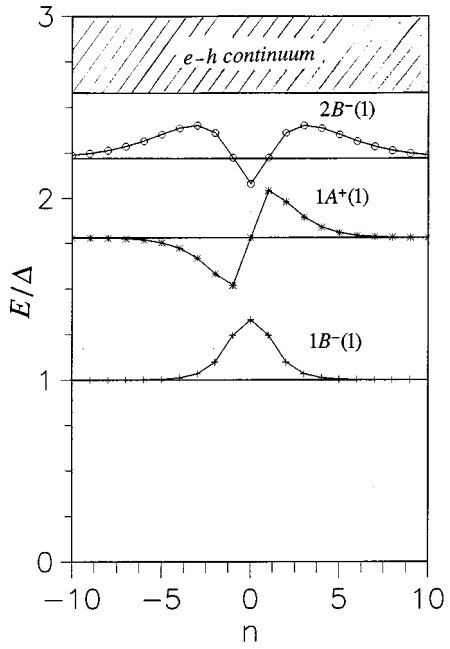

FIG. 3. Energy-level diagram for $\hat{H}_1$, calculated numerically for $\alpha=0.9$, $\beta=0.2$, $\Delta/V_0=0.5$, and $N=101$. Only three of the lowest-energy bound states and the electron-hole continuum are shown. The corresponding wave functions for the bound states are also shown as a function of the electron-hole distance, n.

this reduces the number of states by a factor of N. The remaining four particle eigenstates can be expanded as

$$\sum_{p=1}^{N}\sum_{q=1}^{(N-1)/2}\sum_{j=1}^{N-1}\sum_{k=j+1}^{N} a_{q;j,k}d_p^\dagger d_{p+q}^\dagger c_{p+j}^\dagger c_{p+k}^\dagger|G\rangle, \tag{20}$$

where p indicates the position of the first hole and q is the distance between the two holes, j and k (with $k>j$) index the electron positions relative to the first hole. With N odd, the total number of independent qjk states is therefore $N(N-1)^2/4$. We can further isolate the two-photon allowed eigenstates, denoted $mA^+(2)$, which have even symmetry upon reflection and charge conjugation through the expansion:

$$mA^+(2)=\sum_{p=1}^{N}\sum_{q=1}^{(N-1)/2}\sum_{j=1}^{N-1}{\sum_{k=j+1}^{N}}' a_{q;j,k}^{(m)}(1+\hat{R})\times(1+\hat{Q})d_p^\dagger d_{p+q}^\dagger c_{p+j}^\dagger c_{p+k}^\dagger|G\rangle. \tag{21}$$

The prime indicates that the summation in Eq. (21) is restricted to states $(q;j,k)$ that are not related by $\hat{R}$, $\hat{Q}$, or $\hat{R}\hat{Q}$. Thus the number of two-photon allowed eigenstates is further reduced by approximately a factor of four, to $N^3/16$. At this size we can numerically diagonalize $\hat{H}_2$ for N as high as 31. At this size there are already close to 2000 basis functions of the form of Eq. (21).

A. The small-β limit

When $\beta \ll \alpha(1)-\alpha(2)=\alpha/2$, the lowest-energy states with one or two e-h pairs are tightly bound, with the electron-hole separation limited to at most one lattice spacing. This leads

to an enormous reduction in the one and two e-h pair basis sets extending our analysis to polymers with several hundred unit cells.

States with a single e-h pair can easily be calculated analytically. The states in Eqs. (18) and (19) can be expanded in a basis set that includes only one-exciton bond (or Frenkel) states and nearest-neighbor charge-transfer (CT) states. The three relevant basis functions are

$$|b\rangle \equiv N^{-1/2}\sum_{p=1}^{N} d_p^\dagger c_p^\dagger |G\rangle, \tag{22a}$$

$$|+-\rangle_k \equiv \sqrt{2/N}\sum_{p=1}^{N} \cos\left[\frac{k\pi(2p+1)}{N}\right] d_p^\dagger c_{p+1}^\dagger |G\rangle, \tag{22b}$$

$$|-+\rangle_k \equiv \sqrt{2/N}\sum_{p=1}^{N} \cos\left[\frac{k\pi(2p-1)}{N}\right] d_p^\dagger c_{p-1}^\dagger |G\rangle,$$

$$k=0,1,..,N-1, \tag{22c}$$

the first being the bond exciton and the latter the nearest-neighbor CT excitons. These states are connected via the charge transfer part of $\hat{H}_1$ in (1). Diagonalizing the subspace gives the three eigenstates:

$$1A^+(1) = \frac{1}{\sqrt{2}}(|+-\rangle_1 - |-+\rangle_1), \tag{23a}$$

$$1B^-(1) = c_1|b\rangle + c_2(|+-\rangle_0 + |-+\rangle_0), \tag{23b}$$

$$2B^-(1) = c_2|b\rangle - c_1(|+-\rangle_0 + |-+\rangle_0), \quad \beta \ll 1,\alpha, \tag{23c}$$

with $c_1=\lambda/[\lambda^2+8\beta^2]^{1/2}$ and $c_2=2^{3/2}\beta/[\lambda^2+8\beta^2]^{1/2}$ with $2\lambda \equiv 1-\alpha+[(1-\alpha)^2+32\beta^2]^{1/2}$. The corresponding energies (in units of V_0) are

$$E_{1B^-(1)} = \Delta/V_0, \tag{24a}$$

$$E_{2B^-(1)} = \Delta/V_0 + \sqrt{(1-\alpha)^2+32\beta^2}, \tag{24b}$$

$$E_{1A^+(1)} = \Delta/V_0 + \tfrac{1}{2}\{(1-\alpha)+\sqrt{(1-\alpha)^2+32\beta^2}\},$$

$$\beta \ll 1,\alpha, \tag{24c}$$

where the one-exciton transition energy is $\Delta = e_e + e_h - (V_0/2)\{(1+\alpha)+\sqrt{(1-\alpha)^2+32\beta^2}\}$. Actually, β should be replaced by $\beta\cos(2\pi/N)$ in Eq. (24c) but the error induced by neglecting the cosine vanishes as N approaches large values defining the polymer limit.

At $\beta=0$ the $2B^-(1)$ and $1A^+(1)$ states are degenerate. As β increases the degeneracy is lifted with the $1A^+(1)$ state lower in energy than the $2B^-(1)$ state. The energies of the three states are ordered as follows:

$$E_{1B^-(1)} \leqslant E_{1A^+(1)} \leqslant E_{2B^-(1)}. \tag{25}$$

The ordering is actually independent of β being small and is a general property of H_1.

Unfortunately, similar analytical results in the double electron-hole subspace (where electrons and holes *within a given pair* are limited by at most one lattice spacing) are far more challenging to derive. This is essentially because the basis set, although drastically reduced in size, is still quite large, including double-bond excitons, mixed bond-charge transfer excitons, and double charge transfer excitons. However, the basis set size is now of $O[N]$ so that diagonalization of $\hat{H}_2$ can easily proceed for N of several hundred. In what follows we will refer to this basis set as the *truncated* or *reduced* basis set.

V. BIEXCITONS AND TWO-EXCITONS

One-excitons or just excitons are states that are localized in the electron-hole separation coordinate but are delocalized with respect to the center-of-mass coordinate. We define biexcitons as states consisting of two electrons and two holes with a delocalized center of mass but with localization in the hole-hole relative coordinate. Localization with respect to the hole-hole distance leads naturally to their description as excitonic molecules because of the analogy with a homonuclear diatomic molecule. States with two excitons that are delocalized with respect to the hole-hole distance are referred to as *two-excitons*. In this section we derive the conditions under which biexcitons are formed.

We focus only on states with A^+ symmetry and exclude from the subsequent analysis the ''dark'' biexcitons. The two-photon allowed A^+ states are found by diagonalizing the A^+ subblock of $\hat{H}_2$ having zero center-of-mass momentum. This block has approximately $N^3/16$ four-particle basis functions of the form (21). With 64 Mbytes of RAM computer memory the diagonalization was limited to sizes of at most $N=31$. The far smaller $B^-(1)$ subblock, consisting of approximately N basis functions with zero center-of-mass momentum, was also numerically diagonalized in order to evaluate the biexciton binding energy.

In one dimension and for any $V_0>0$ no matter how small, $1B^-(1)$ is a bound state of one electron and one hole. We can then calculate the biexciton binding energy by evaluating $\Delta E_{mA^+(2)}$, defined as

$$\Delta E_{mA^+(2)} \equiv E_{mA^+(2)} - 2E_{1B^-(1)}, \tag{26}$$

where the subscripts on the energy terms have been altered in an obvious way from those in Eq. (10) by including the symmetry labels. The superscript then becomes redundant and is omitted. A negative value, $\Delta E_{mA^+(2)}<0$, indicates the existence of a bound exciton pair or biexciton, $mA^+(2)$, with binding energy $|\Delta E_{mA^+(2)}|$. To show that this condition coincides with localization in the hole-hole relative coordinate, we plot in Fig. 4 the probability of finding the two holes a distance q apart, $P_m(q)$, in the state $mA^+(2)$ at several values of $\Delta E_{mA^+(2)}$. The normalized distribution $P_m(q)$ is averaged over the electron positions and is given by

$$P_m(q) \equiv \sum_{j=1}^{N-1}\sum_{k=j+1}^{N} |a_{q;jk}^{(m)}|^2. \tag{27}$$

As Fig. 4 shows, when $\Delta E_{mA^+(2)}>0$ the probability increases with separation, characteristic of the delocalized *two-exciton* state. When $\Delta E_{mA^+(2)}<0$, $P_m(q)$ becomes localized. The peak in $P_m(q)$ can be associated with the bond distance of the $mA^+(2)$ excitonic molecule. Figure 4 shows

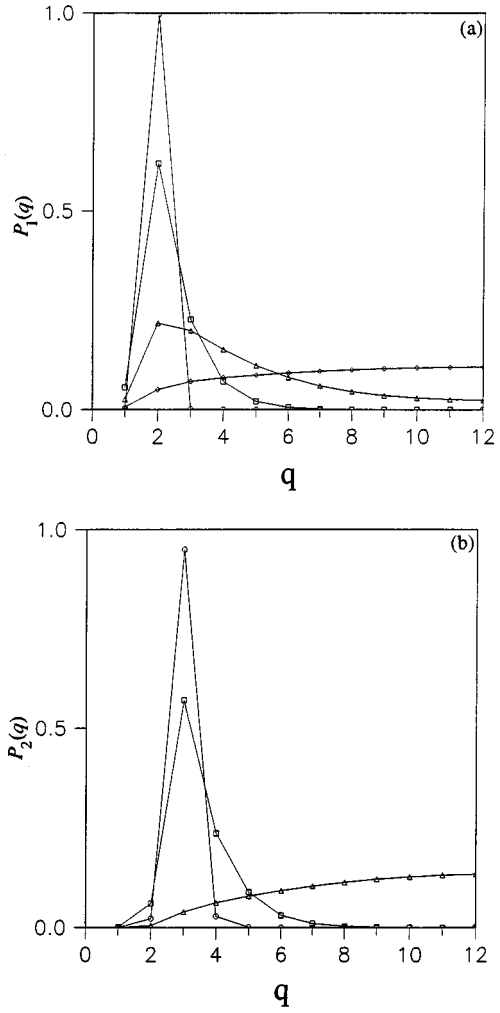

FIG. 4. The hole-hole correlation function, $P_m(q)$ vs q. In (a) $P_1(q)$ corresponding to the state $1A^+(2)$ is shown for $\Delta=V_0$, $\alpha=1$ and four values of β: $\beta=0.01$ (circles), $\beta=0.075$ (squares), $\beta=0.10$ (triangles), and $\beta=0.12$ (diamonds). The corresponding values of $\Delta E_{1A^+(2)}$ are -0.277, -2.6×10^{-2}, -2.9×10^{-3}, and $+3.4\times10^{-4}$, respectively. In (b) $P_2(q)$ corresponding to the state $2A^+(2)$ is shown for $\Delta=V_0$, $\alpha=1$ and three values of β: $\beta=0.01$ (circles), $\beta=0.02$ (squares), and $\beta=0.03$ (triangles). The corresponding values of $\Delta E_{2A^+(2)}$ are -3.3×10^{-2}, -4.8×10^{-3}, and $+1.7\times10^{-4}$. All curves were calculated with $N=25$ cells and the full basis set.

the evolution of the lowest-energy $1A^+(2)$ biexciton as well as the higher-energy $2A^+(2)$ biexciton. In both cases localization increases with biexciton binding energy. The $1A^+(2)$ biexciton is eventually localized near $q=2$ while the $2A^+(2)$ biexciton localizes near $q=3$.

Generally, the total (dimensionless) biexciton energy depends on Δ/V_0, α, and β. In what follows, we investigate the parameter ranges over which biexcitons exist. The problem is greatly simplified by recognizing that the biexciton binding energy, from Eqs. (10) and (26) is

$$\Delta E_{mA^+(2)}=f_{mA^+(2)}(\alpha,\beta)-2\,f_{1B^-(1)}(\alpha,\beta) \tag{28}$$

for the mth biexciton. Thus $\Delta E_{mA^+(2)}=0$, which defines the biexciton phase boundaries, depends only on α and β. This

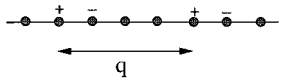

FIG. 5. The relative arrangements of two electrons and two holes for a biexciton candidate when $\beta=0$. The cells without an indicated charge are in their ground state (σ^2). The $q=4$ case shown is bound relative to two free $1B^-(1)$ excitons whenever, according to Eq. (31), $\alpha>60/61$.

makes sense from a wave-function point of view since the eigenstates of $\hat{H}_2$ depend only on α and β.

To appreciate the nature of the phase diagram in (α,β) space, and in particular how many biexcitons are to be expected, we begin with the simple case with $\beta=0$, where the local states in Eqs. (18)–(21) are now the eigenstates. There is a single one-photon allowed one-exciton state, $1B^-(1)=(1/\sqrt{N})\Sigma_{p=1}^{N}d_p^\dagger c_p^\dagger|G\rangle$, with energy $\Delta\equiv V_0E_{1B^-(1)}=e_e+e_h-V_0$. Given the $1/r$ potential in Eq. (3) and the restriction $\alpha\leqslant1$, the only candidates for biexciton states are those depicted graphically in Fig. 5. They consist of two nearest-neighbor charge transfer states in which the hole-hole distance as well as the electron-electron distance is q. (Any other arrangement of electrons and holes will necessarily have $\Delta E_{mA^+(2)}>0$ for $\alpha\leqslant1$.) One-half of these states have A^+ symmetry and are written as

$$(q-1)A^+(2)=\frac{1}{\sqrt{2N}}\sum_{p=1}^{N}\{d_p^\dagger d_{p+q}^\dagger c_{p+1}^\dagger c_{p+q+1}^\dagger - d_p^\dagger d_{p+q}^\dagger c_{p+q+N-1}^\dagger c_{p+N-1}^\dagger\}|G\rangle,$$

$$q=2,3,\ldots, \tag{29}$$

$$\beta=0,$$

with energies

$$E_{(q-1)A^+(2)}=2\left\{\frac{\Delta}{V_0}+1-\frac{1+(q-1)q(q+1)}{(q-1)q(q+1)}\,\alpha\right\},$$

$$q=2,3,\ldots, \tag{30}$$

$$\beta=0.$$

To find which of these states are biexcitons one needs to evaluate $\Delta E_{(q-1)A^+(2)}$ using Eq. (26), and force the right-hand side (rhs) to be negative. This leads to a condition on α,

$$\alpha>\frac{(q-1)q(q+1)}{1+(q-1)q(q+1)},\quad \beta=0 \tag{31}$$

for which the state $(q-1)A^+(2)$ is a biexciton. The lowest-energy state $1A^+(2)$ $(q=2)$ is therefore a biexciton when $\alpha>6/7\approx0.857$, while the next highest state $2A^+(2)$ is a biexciton $(q=3)$ when $\alpha>24/25=0.96$, and so on. This is consistent with Fig. 4, which shows that as β decreases the low-

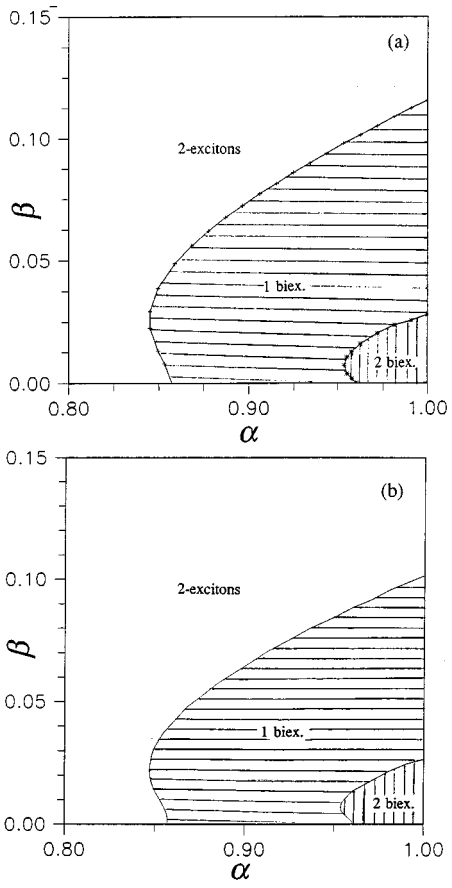

FIG. 6. The biexciton phase space showing two phase boundaries (see text). The phase boundaries were calculated numerically by solving $\Delta E_{1A^+(2)}=0$ and $\Delta E_{2A^+(2)}=0$ for $N=25$ using the full basis set (6a) and the truncated basis set (6b) under the small-β limit. In the region labeled 2 biex. there are *at least* two biexcitons since it encompasses successively smaller regions containing at least 3 biexcitons, 4 biexcitons, etc., which are not shown.

est two biexcitons localize on $q=2$ and $q=3$, respectively. Note that when $\alpha=1$, the infinite chain supports an infinite number of biexcitons, with binding energies that vanish as q tends to infinity.

We now turn to the general question of biexciton existence over the complete (α,β) space. Intuitively, one might expect that increasing β dissociates biexcitons. The more tightly bound biexcitons near $\alpha=1$ would survive larger values of β. For α slightly greater than $\frac{6}{7}$ a vanishingly small value of β might be expected to dissociate the biexciton. To test these predictions we numerically calculated the biexciton phase diagram. The phase boundary for the mth biexciton is a solution of $\Delta E_{mA^+(2)}=0$. Figure 6 shows the phase boundaries calculated for a chain of $N=25$ sites using the full basis set [Fig. 6(a)] and the reduced basis introduced in Sec. IV for small β [Fig. 6(b)]. $N=25$ is large enough to ensure convergence of the lowest biexciton energies to their polymer values to within approximately 5% over the entire phase boundary. This was checked by calculating the phase boundary for smaller sizes in the full basis set and observing convergence. For example, in the small-beta limit, where much larger sizes can be studied, the $\alpha=1$ intercept changes by less than 3% when N is increased to 100. The diagram only applies to states with A^+ symmetry. Furthermore, only two of the many phase boundaries are shown: one that divides the region of delocalized two-excitons and the region where only the $1A^+(2)$ biexciton exists, and one that divides the latter region from one that supports two biexcitons, $1A^+(2)$ and $2A^+(2)$. Boundaries separating the m and $(m+1)$ biexciton regions, with $m>1$ are not shown. They occupy successively smaller regions in phase space and are centered at $\alpha=1$ and $\beta=0$.

Figure 6 shows that the small β approximation is a good one over the entire biexciton phase space. The largest deviation occurs near the $\alpha=1$ intercept of the $1A^+(2)$ phase boundary, with the truncated basis set calculation underestimating the intercept by about 15%. The $\beta=0$ intercepts agree in both calculations with the analytical results given by Eq. (31). The figure shows that the $1A^+(2)$ biexcitons are dissociated with increasing β over most of the range $6/7\leqslant\alpha\leqslant1$ as expected. A notable exception occurs near $\alpha=\frac{6}{7}$. Surprisingly, $1A^+(2)$ biexcitons exist even when α is slightly *less* than $\frac{6}{7}$; increasing β in this region initially leads to the creation of a biexciton; i.e., it enhances the binding of two excitons. The unusual behavior stems from a resonance effect. When $\alpha=\frac{6}{7}$ and $\beta=0$, the binding energy of the $1A^+(2)$ state from Eqs. (26) and (30) with $q=2$ is zero. This state is degenerate with the $(N-1)/2$ eigenstates of the form

$$\frac{1}{\sqrt{N}}\sum_{p=1}^{N} d_p^\dagger d_{p+q}^\dagger c_p^\dagger c_{p+q}^\dagger |G\rangle, \quad q=1,2,\ldots,(N-1)/2, \tag{32}$$

which consist of two noninteracting bond excitons (electrons and holes are paired on the same sites). Degenerate perturbation theory shows that $1A^+(2)$ and the noninteracting bond excitons are mixed at zero order, significantly lowering the energy of the bound state for nonzero β. Thus, increasing β near $\alpha=\frac{6}{7}$ leads to an increase in the $1A^+(2)$ biexciton binding energy. An identical argument applies to the higher biexcitons with the unusual behavior appearing near the points α given by the rhs of Eq. (31) with $q>2$.

Figure 7 shows how the biexciton binding energy $|\Delta E_{1A^+(2)}|$ varies over the biexciton phase space. The binding energy peaks at $(\alpha=1,\ \beta=0)$ with $|\Delta E_{1A^+(2)}|=0.33$ from Eqs. (26) and (30), and decreases steadily as one moves into the biexciton phase space. Near $\alpha=\frac{6}{7}$ the (minute) binding energy increases with β over a range $\beta=0.01$–0.02 due to the aforementioned resonance effect. Figures 6 and 7 show that no biexcitons are possible when β surpasses approximately 0.11, or when α is less than approximately 0.845.

VI. TWO-PHOTON ABSORPTION SPECTRA

The biexcitons of the last section can be observed through the technique of two-photon absorption. The absorption of a laser beam of frequency ω is enhanced whenever 2ω is in resonance with the biexciton transition frequency, $V_0E_{mA^+(2)}/\hbar$. In this section we calculate TPA in the spectral region $2\hbar\omega<2\Delta$ for the 1D polymer with the Hamiltonian (4). In this range we avoid one-photon resonances to one-exciton states. Furthermore, we limit our analysis to the phase space near or within the biexciton existence region, where β is small ($\beta<0.11$) and less than α. The resulting excitons and biexcitons are therefore tightly bound with radii much smaller than the total polymer length, $N=25$, used in

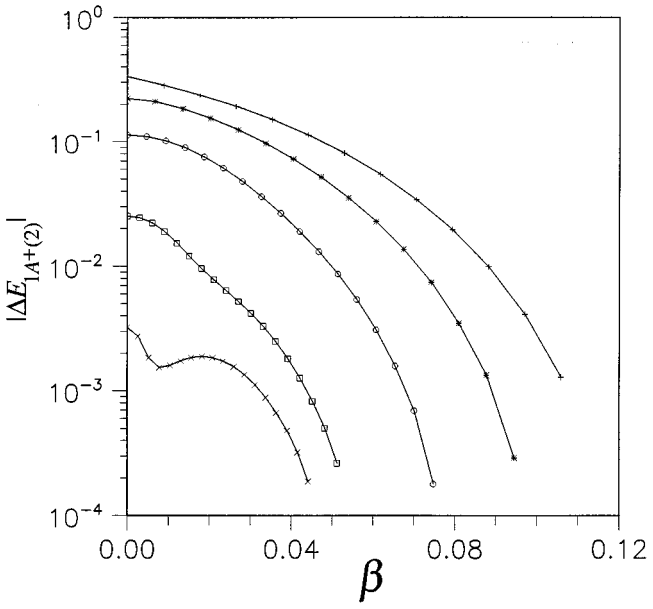

FIG. 7. Biexciton binding energy, $|\Delta E_{1A^+(2)}|$ calculated using the full basis set for $N=25$ as a function of β for several values of α: $\alpha=1$ (crosses), $\alpha=0.95$ (asterisks), $\alpha=0.91$ (circles) $\alpha=0.868$ (squares), and $\alpha=0.859$ (diagonal crosses). The energies are dimensionless and in units of V_0.

our full-basis calculations. At this size, the wave functions and energies are converged to their polymer values.

In addition to $mA^+(2)$ biexciton peaks there may also be peaks arising from the two-photon allowed single exciton states, $mA^+(1)$. Since the symmetry of these states guarantees a node at $n=0$ (n being the electron-hole separation) they have total charge transfer character. Hence we refer to these states as CT excitons from here on. In this section we explore the relationship between these peaks.

Two-photon absorption is a third-order process governed by the imaginary part of the nonlinear susceptibility $\chi^{(3)}_{ijkl}(-\omega;\omega,\omega,-\omega)$. For a sample consisting of randomly oriented chains (as is the case for most polymer films) and for light polarized along the x axis, only the component $\chi^{(3)}_{xxxx}$ contributes to the response. If we ignore the transverse response of an individual chain, $\chi^{(3)}_{xxxx}$ is related to the individual chain (second) hyperpolarizability, γ_{xxxx}, by

$$\chi^{(3)}_{xxxx}=\tfrac{1}{5}L(\sigma/Na)\,\gamma_{xxxx}, \tag{33}$$

where the factor of $\frac{1}{5}$ comes from the orientational average, L is a local field factor and σ is the number of chains per unit area. The two-photon absorption *per site* in a given chain is obtained by taking the large-N limit of $\mathrm{Im}[\gamma_N/N]$, where, from here on γ represents γ_{xxxx}. For incident light detuned far to the red of any one-photon resonances we get[25]

$$\mathrm{Im}[\gamma_N(-\omega;\omega,\omega,-\omega)]$$
$$=8\sum_{I=1}^{2}\sum_{l,m,n}\frac{h(I)\Gamma_{mA^+(I)}\langle G_0|\hat{\mu}_x|lB^-(1)\rangle\langle lB^-(1)|\hat{\mu}_x|mA^+(I)\rangle\langle mA^+(I)|\hat{\mu}_x|nB^-(1)\rangle\langle nB^-(1)|\hat{\mu}_x|G_0\rangle}{(E_{lB^-(1)}-\hbar\omega)(E_{nB^-(1)}-\hbar\omega)[(E_{mA^+(I)}-2\hbar\omega)^2+\Gamma^2_{mA^+(I)}]}, \tag{34}$$

where $2\Gamma_{mA^+(I)}$ is the inverse radiative lifetime of the state $mA^+(I)$, with $I=1,2$. An additional factor of two for the electron spin degeneracy is included in Eq. (34). The first summation is over the two main pathways, which contribute to the TPA. They can be schematically depicted as

$$G\rightarrow mB^-(1)\rightarrow nA^+(1)\rightarrow m'B^-(1)\rightarrow G \quad [\text{pathway } (1)],$$

$$G\rightarrow mB^-(1)\rightarrow nA^+(2)\rightarrow m'B^-(1)\rightarrow G \quad [\text{pathway } (2)],$$

corresponding to the $I=1$ and $I=2$, respectively in Eq. (34). Each state is connected via a transition dipole matrix element. In the range $2\hbar\omega<2\Delta$ pathway (1) represents two-photon absorption to CT exciton states $mA^+(1)$, while pathway (2) represents two-photon absorption to biexcitons $mA^+(2)$. In the complete expression for $\gamma_N(-\omega;\omega,\omega,-\omega)$ there is an additional pathway that involves four transitions between the ground state and the one-exciton states. Such a contribution is nonresonant and therefore negligible in the spectral range $2\Delta-2\hbar\omega\gg\Gamma_{1B^-(1)}$, which is assumed in Eq. (34).

The transition dipole matrix elements that connect the states in pathways (1) and (2) originate from either the first or second terms in Eq. (11). In pathway (1) the first and fourth transitions are interband ones, while the intermediate two are intraband. In pathway (2) all transitions are interband. The form of the intraband component in Eq. (11) is adapted to a ring; in order to correct for a straight polymer we have to multiply the $I=1$ contribution in Eq. (34) by an extra factor of two. This offsets the factor of $\frac{1}{2}$, which is inherent in averaging of $\sin^2[2\pi p/N]$ (from the intraband dipole moment squared) over all p. The $h(I)$ factor accounts for this: $h(1)=2$ and $h(2)=1$.

We have verified numerically that the per-site response $N^{-1}\mathrm{Im}[\gamma_N(-\omega;\omega,\omega,-\omega)]$ using Eq. (34) converges as N is taken to large values. This was shown rigorously in Ref. 21 for the case of nonresonant susceptibilities, and the limiting

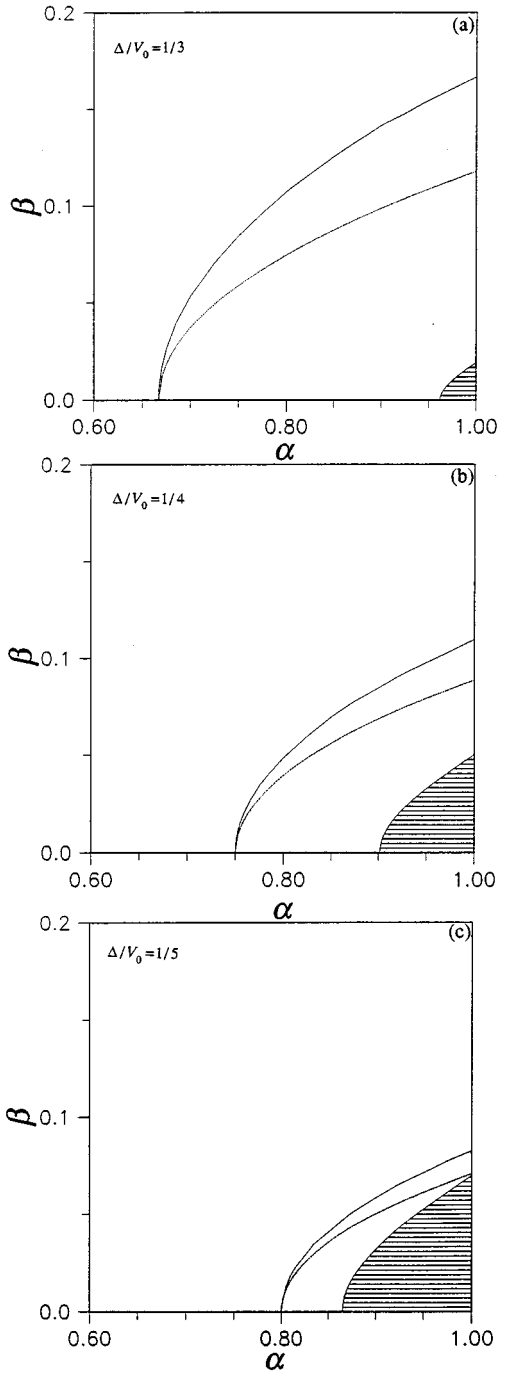

FIG. 8. The $1A^+(1)$ crossover curves calculated numerically for the full basis set with $N=101$ (solid line) and analytically from Eq. (36) (dashed line) for several values of $\Delta/V_0=\frac{1}{3},\frac{1}{4},\frac{1}{5}$. In all cases the analytical curves underestimate the exact numerical results. Also shown is the CDW ground-state region.

values were derived analytically in the regimes of weak and strong localization. Before using Eq. (34) to calculate TPA spectra we turn to a simpler endeavor and answer the following question. For values of α and β within the biexciton phase space are there additional TPA peaks arising from the higher CT excitons? In other words under what ranges of α and β can we expect pathways (1) and (2) to contribute to the TPA spectrum?

The solution can be obtained by straightforward numerical analysis. For a given value of Δ/V_0 the quantity

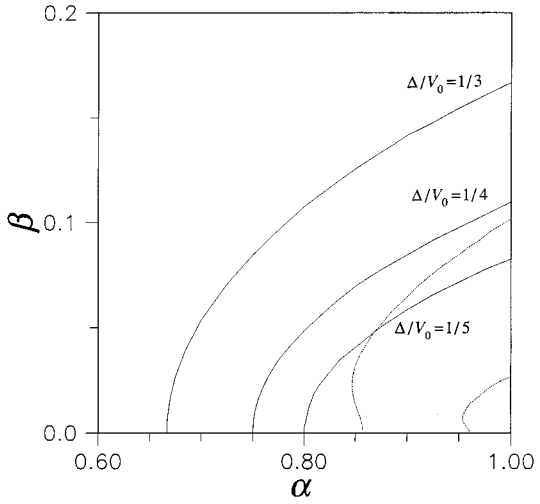

FIG. 9. The crossover curves (solid lines) for several values of Δ/V_0 along with the biexciton phase boundaries (dashed lines).

$$\Delta E_{\mathrm{CT}} \equiv E_{1A^+(1)} - 2\Delta/V_0 \tag{35}$$

is evaluated. $\Delta E_{\mathrm{CT}}=0$ is a curve in (α,β) space that includes the points at which the energy of the $1A^+(1)$ CT exciton peak crosses over into the range $\Delta<V_0E_{1A^+(1)}<2\Delta$. When $\Delta E_{\mathrm{CT}}<0$, which corresponds to all points under the curve, there is an additional peak arising from the CT exciton state $1A^+(1)$ in the region $\Delta<2\hbar\omega<2\Delta$, and possibly more peaks from the $mA^+(1)$ states with $m>1$. When $\Delta E_{\mathrm{CT}}>0$ these peaks are shifted beyond 2Δ. Figure 8 shows such crossover curves for several values of Δ/V_0 along with the CDW phase region.

For small β the crossover curves can be derived analytically by using the energies in Eq. (24). Inserting Eq. (24) into Eq. (35) the condition $\Delta E_{\mathrm{CT}}<0$ becomes

$$8\beta^2 - \frac{\Delta}{V_0}\,\alpha < \frac{\Delta}{V_0}\left(\frac{\Delta}{V_0}-1\right), \quad \beta \ll \alpha, \tag{36}$$

as the condition under which the TPA peak lies in the gap. The $\Delta E_{\mathrm{CT}}=0$ curves, obtained by making Eq. (36) an equality, are then simply parabolas. These are also shown in Fig. 8.

Figure 9 shows the crossover curves for several values of Δ/V_0 as well as the $m=1$ and $m=2$ biexciton phase boundaries. When $\Delta/V_0=1/5$ the crossover curve intersects the $(m=1)$ biexciton phase boundary. In the region where the biexciton phase space overlaps the area under the crossover curve, $1A^+(2)$ biexcitons and $mA^+(1)$ excitons will contribute TPA peaks in the range $2\hbar\omega<2\Delta$. As Δ/V_0 increases, the crossover curves shift to the left, eventually completely enclosing the biexciton phase space; here we expect biexciton peaks will always be accompanied by CT exciton peaks.

Using Eq. (34) we now evaluate the TPA spectra in various regions of the biexciton phase space. We start along a horizontal cut in (α,β) space keeping $\beta=0.01$ constant and taking $\Delta/V_0=0.40$, so that the phase space is devoid of CDW's [see Eq. (14)]. According to Fig. 9 the CT exciton crossover curve completely encloses the biexciton phase space, so that the biexciton peak, if present, will always be accompanied by a CT exciton peak. Figure 10 shows TPA

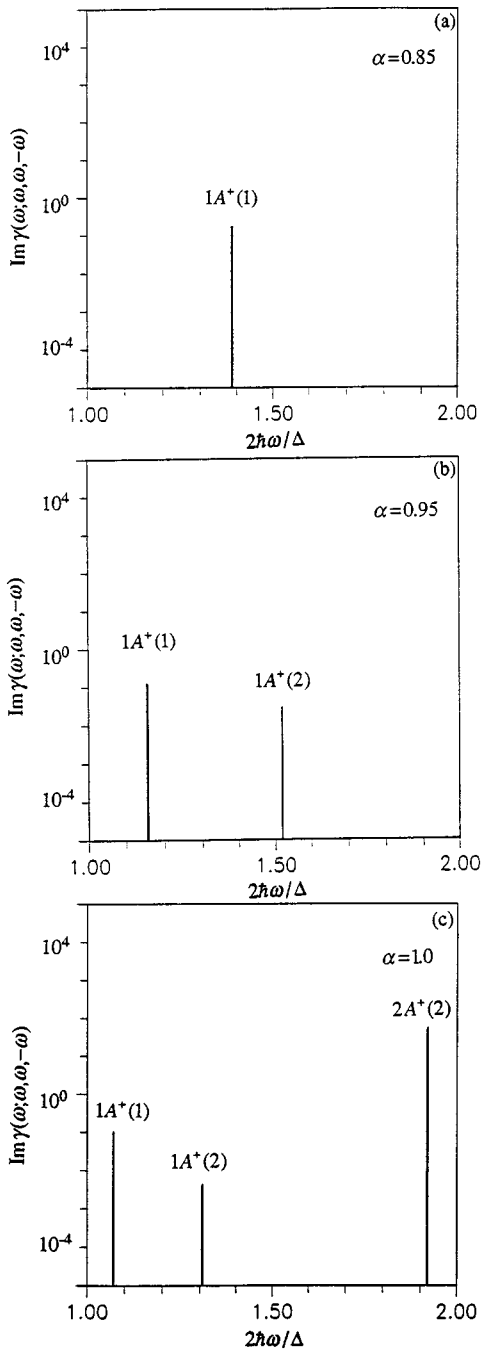

FIG. 10. TPA spectra (in arbitrary units) at three points along a horizontal cut (β=0.01) in phase space. The stick figure spectra are obtained from Eq. (34) in the limit of small Γ with all $\Gamma_{mA^+(1)}=\Gamma$. In all cases N=25, $\mu_c=ea/2$, and $\Delta/V_0=0.4>2\ln 2-1$, so that CDW's do not exist at any point (α,β). The solid sticks are full basis-set calculations while the hollow sticks are truncated basis-set calculations in the small-β limit. In all cases the two calculations cannot be distinguished.

spectra at three points along the cut. The first point (α=0.85, β=0.01), is outside the $1A^+(2)$ biexciton phase region of Fig. 6, but is below the $\Delta/V_0=\frac{1}{3}$ crossover curve in Fig. 8, indicating that only CT excitons contribute TPA peaks. Figure 10(a) shows a single CT exciton peak. At these small values of β the tightly bound exciton approximation of the last section is valid. Using Eq. (24b) we get

$$V_0E_{1A^+(1)}\approx 1.38\Delta,$$

which is in excellent agreement with the numerical value, as shown in Fig. 10(a). The TPA intensity corresponding to pathway (1) can be derived analytically in the small β limit. Using Eqs. (11) and (23), the result is

$$\text{pathway}(1)\propto\frac{\beta^2}{(1-\alpha)^2+32\beta^2}\left[\frac{1}{(E_{1B^-(1)}-E_{1A^+(1)}/2)^2}+\frac{1}{(E_{2B^-(1)}-E_{1A^+(1)}/2)^2}-\frac{2}{(E_{1B^-(1)}-E_{1A^+(1)}/2)(E_{2B^-(1)}-E_{1A^+(1)}/2)}\right],$$

which yields intensities that are in excellent agreement with those in Fig. 10(a). These analytical expressions also work well for the $1A^+(1)$ feature in Figs. 10(b) and 10(c).

When α is increased to α=0.95 the $1A^+(2)$ biexciton existence region is entered. Figure 10(b) shows two TPA peaks, the low-energy one corresponding to the CT exciton and the higher-energy one corresponding to the $1A^+(2)$ biexciton. Both peaks continue to shift to lower energy as α is increased further. Eventually, the two-biexciton [$1A^+(2)$ and $2A^+(2)$] existence region (see Fig. 6), is entered in Fig. 10(c) when α=1. This is marked by the appearance of a second biexciton peak from the $2A^+(2)$ state. Note that horizontal cuts with smaller values of β will yield greater numbers of biexciton peaks when α=1.

Figure 11 shows the results of a vertical cut in (α,β) space with α=0.95. In this case $\Delta/V_0=\frac{1}{3}$, so that the CT exciton crossover curve again encloses the $1A^+(2)$ biexciton phase space. Along this cut there are no CDW's. This series of spectra demonstrate that as β increases the peak positions are generally blueshifted.

Figures 10 and 11 show that the biexciton peaks as well as the CT exciton peaks always lie in the range $\Delta<2\hbar\omega<2\Delta$. The lower limit on the CT exciton energy follows from the fact that for $\hat{H}_1$ the state $1B^-(1)$ is always lowest in energy. The lower limit for the biexciton is more subtle. It arises because the increase in V_0 necessary to increase the binding energy beyond Δ, would simultaneously create the CDW ground state.

Lastly, we turn our attention to the transition dipole moment from the $1B^-(1)$ state to the most tightly bound biexciton, $1A^+(2)$. Recently, Guo, Chandross, and Mazumdar[18] have suggested that biexcitons can be identified as those states having an energy below the two-exciton continuum 2Δ, with a transition moment from $1B^-(1)$ *less* than that to the band-edge two-exciton state. We investigated this criterion in Figs. 12 and 13, where $|\langle 1B^-(1)|\hat{\mu}_x|mA^+(2)\rangle|$ is shown as a function of the normalized energy $V_0E_{mA^+(2)}/\Delta$. A series of such plots are shown at two cuts in (α,β) space near the $1A^+(2)$ biexciton phase boundary. Figures 12(a)–12(c) display three points along a horizontal cut with constant β=0.01. All three points lie within the biexciton phase space so that the first peak corresponds to the $1A^+(2)$ biexciton and is therefore below 2Δ in all cases. The figure shows that when the biexciton initially splits from the two-exciton continuum, it carries with it more oscillator strength than the band-edge two-exciton state. The situation

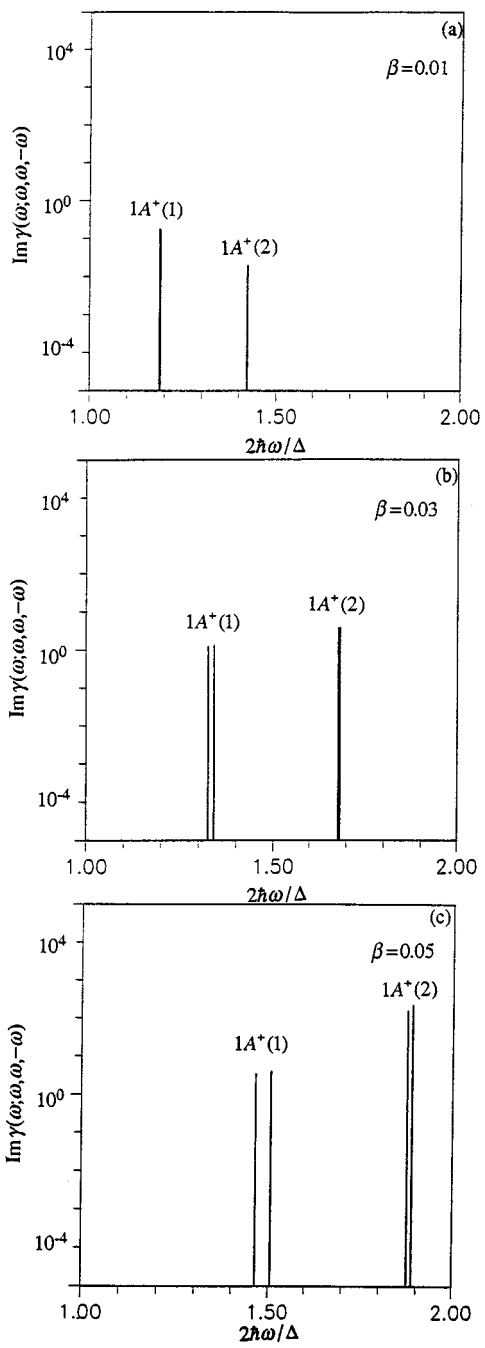

FIG. 11. Same as Fig. 10 except that TPA spectra (in arbitrary units) are taken at three points along a vertical cut (α=0.95) in phase space. The truncated basis set calculations cannot be distinguished from the full basis set calculations in (a), while they are slightly higher in energy in (b) and (c).

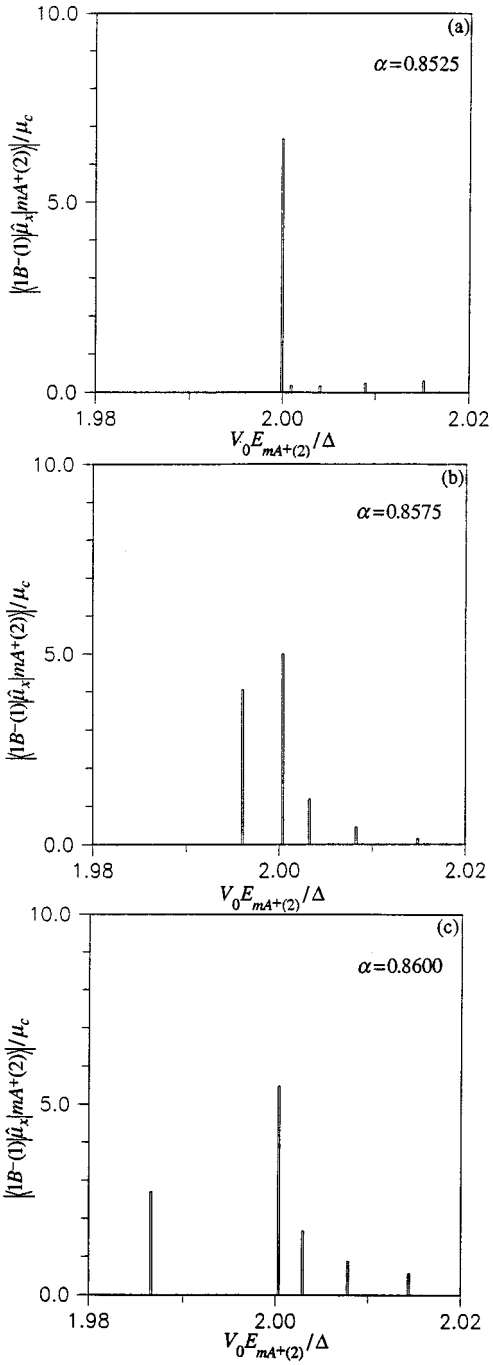

FIG. 12. Magnitude of the exciton-biexciton transition dipole moment, $\langle 1B^-(1)|\hat{\mu}_x|mA^+(2)\rangle/\mu_c$, as a function of the energy $V_0E_{mA^+(2)}/\Delta$ for several points near the $1A^+(2)$ biexciton phase boundary and within the biexciton phase region. In all cases β=0.01 and Δ/V_0=0.2.

reverses as the binding energy increases; eventually the oscillator strength resides primarily in the band-edge two-exciton state as predicted by Guo, Chandross, and Mazumdar.[18] Figures 13(a)–13(c) display three points along a vertical cut with constant α=0.95. Again all three points are just within the $1A^+(2)$ biexciton phase space. The same qualitative behavior is observed as in Fig. 12.

In a tightly bound biexciton with a small radius R, the oscillator strength $|\langle 1B^-(1)|\hat{\mu}_x|mA^+(2)\rangle|^2$ is roughly R/N times that of the band-edge two-exciton state, which is delocalized over all cells. This is because creating a second exciton within a radius R from the first has a probability R/N. However, this argument cannot explain how $|\langle 1B^-(1)|\hat{\mu}_x|mA^+(2)\rangle|^2$ for a weakly bound, large radius biexciton can greatly exceed that of the two-exciton band-edge state as in Figs. 12(a) and 13(a). The problem lies in the assumption that the band-edge two-exciton wave function has site amplitudes that are in-phase; it may contain one or more nodes in the relative coordinate of the two excitons,

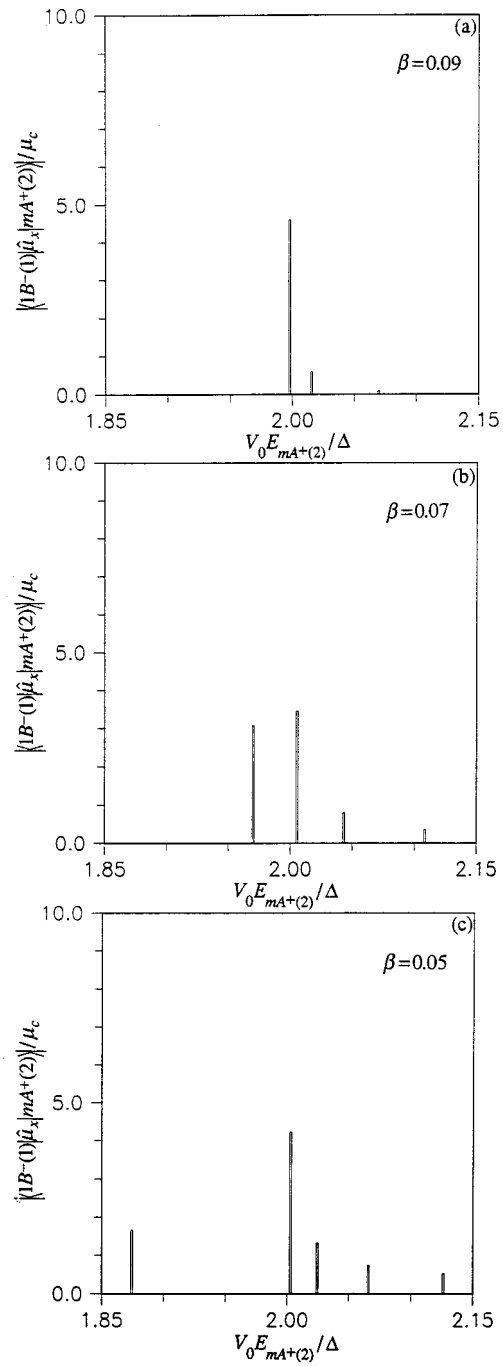

FIG. 13. Magnitude of the exciton-biexciton transition dipole moment, $\langle 1B^-(1)|\hat{\mu}_x|mA^+(2)\rangle/\mu_c$, as a function of the energy $V_0E_{mA^+(2)}/\Delta$ for several points near the biexciton phase boundary and within the biexciton phase region. In all cases $\alpha=0.95$ and $\Delta/V_0=0.33$.

which leads to a substantial reduction in dipole moment, even though it remains completely delocalized. A biexciton state can be expanded in a noninteracting two-exciton basis set, $|K\rangle$, where K is the wave vector corresponding to the relative motion of the two excitons. When a biexciton initially splits from the two-exciton band, it has a large radius and consequently a large $K=0$ (nodeless) component; the remaining two-exciton band-edge state is left with a smaller $K=0$ component. Thus, initially the biexciton captures more of the oscillator strength. As the biexciton becomes more tightly bound it acquires higher wave-vector components, causing the oscillator strength to drop, while the two-exciton band-edge state regains a larger $K=0$ component. Eventually the two-exciton band-edge state recovers enough of the zero mode state to surpass the biexciton in oscillator strength. The same behavior also applies to Frenkel biexcitons[26,27] in linear chains.

VII. DISCUSSION AND CONCLUSION

The two-band tight-binding Hamiltonian in Eq. (4) with the Coulombic potential in Eq. (3) supports multiple biexciton states in limited regions of (α,β) phase space as shown in Fig. 6. Because the Hamiltonian commutes with the total particle number, the biexcitons presented here are well defined, and correspond to states with two electrons and two holes with localization in the hole-hole relative coordinate (see Fig. 4). The shape of the phase boundaries in Fig. 6 sensitively depends on the form of the extended Coulombic potential, which we have taken to be the usual $1/r$ form for $r\geqslant a$. Truncating the interaction to nearest neighbor only $[\alpha(n)=0;\ n>1]$, as in the case of strong screening, for example, increases the binding energy of the $1A^+(2)$ biexciton but eliminates the existence of all higher biexcitons. In this case the $\beta=0$ intercept of the $1A^+(2)$ biexciton phase boundary occurs at $\alpha=\frac{2}{3}$, instead of $\alpha=\frac{6}{7}$ obtained with the extended potential in Eq. (3). Such screening may arise in polymer films where the chain density is high. In this case there may also be interchain biexcitons with one e-h pair per chain. Such a scenario was recently discussed by Soos and Kepler.[6]

Given the form of the Coulombic potential, the existence of biexcitons depends only on the parameters α and β, while the existence of the CDW ground state depends on α, β, and Δ/V_0 (see Fig. 2). A CDW is *possible* only when $\Delta<(2\ln 2-1)V_0$, or when the on-site electron-electron repulsion V_0 exceeds 2.6 times the energy Δ of the lowest one-photon allowed state, $1B^-(1)$. As V_0 increases above this limit the CDW region occupies an increasingly larger corner of phase space centered on ($\alpha=1$, $\beta=0$), but as long as it is completely enclosed by the biexciton phase boundary it is possible to discuss TPA to biexcitons from the neutral ground state G_0 in the region that avoids the CDW. We note that Ostreich and Schonhammer[22] intentionally avoided the CDW region by diagonalizing the same Hamiltonian in Eq. (2) for $\alpha<1/2\ln 2\approx 0.72$. Their large-scale numerical calculations showed no stable biexcitons, a result consistent with our own calculations, which show biexcitons only when $\alpha\gtrsim 0.845$.

The ordering $E_{1B^-}<E_{1A^+}$ is a general property of $\hat{H}_1$ and is consistent with experimental findings for PS and PPV. An important limitation of our model is its inability to account for the reverse ordering that occurs in weakly alternating polymers such as polyacetelylene. Recently Mukhopadhyay, Hayden, and Soos[11] analyzed dimerized PPP and Hubbard chains and studied in detail the spin-charge crossover over a range of parameters. Their treatment is exact, taking full account of the spin statistics and limited to at most seven dimers. On the band side of the crossover region ($E_{1B_u}<E_{2A_g}$) calculations for large alternations ($\delta=0.6$) show that the lowest excited state under the PPP Hamiltonian has

strong bond exciton character while two-photon allowed excited states have largely charge-transfer character, in agreement with our results. However, unlike the present treatment, they also include a two-photon allowed excited state within the dimer cell that contributes to the biexciton near $2E_{1B^-}$. An obvious extension of the current model is to include this state. Recently, Knoester and Spano[28] studied TPA in a linear chain of coupled three-level systems where the second and third levels are respectively one- and two-photon allowed.

There is some experimental evidence supporting biexcitons in PDA (Ref. 1) and a much greater amount in PS.[3–6] This comes mainly through the existence of a redshifted induced absorption peak in differential pump-probe absorption experiments[1,3–5] and from a high-energy peak in the TPA spectrum.[6] The TPA spectrum of polysilane shows a broad peak at about 1.8Δ ($\Delta \approx 3.4$ eV) as well as a much narrower peak at about 1.3Δ.[6] The low-energy peak has been attributed to the A_g CT exciton state[12,14] while the high-energy peak may be a biexciton.[3–6] Both features are roughly the same magnitude in intensity. Parameters in our model can be found that reproduce these spectral features; for example, Fig. 11(b) shows approximately this spectrum, and a better fit can be obtained by using $\beta=0.04$ instead of $\beta=0.03$ and $\Delta=0.40V_0$ instead of $\Delta=0.33V_0$. Then, $\alpha=0.95$ and the experimental value $\Delta \approx 3.4$ eV gives $t=0.34$ eV, $V_0=8.5$ eV, and $V_1=8.1$ eV. The value of t is close to the value of 0.5 eV obtained from photoelectron spectra of methylated polysilanes.[29] Since the e-h interaction parameters correspond to σ and σ^* molecular orbitals it is difficult to compare with the accepted atomic parameters used in the Ohno potential, for example.[10–12] The most critical parameter is the value of α, which under the extended potential in Eq. (3b), must be larger than about 0.84 to have biexcitons at all. However, the cutoff can be significantly lowered, as previously mentioned, to 0.67 using the screened potential [$\alpha(n)=0$, $n>1$]. We note that Ishida, Aoki, and Chikyu[30] in analyzing the same Hamiltonian as ours used $\alpha=0.80$ in modeling polysilane. Currently we are exploring the existence of biexcitons for other potentials and in cases without charge conjugation symmetry.

ACKNOWLEDGMENTS

Acknowledgments are made to the National Science Foundation through NSF-DMR9312029, for support of this research. We thank Z. G. Soos for many stimulating discussions.

[1] M. Yoshizawa, Y. Hattori, and T. Kobayashi, Phys. Rev. B **47**, 3882 (1993).
[2] M. Chandross, F. Guo, and S. Mazumdar, Synth. Met. **69**, 625 (1995).
[3] J. R. G. Thorne, Y. Ohsako, R. M. Hochstrasser, and J. M. Zeigler, Chem. Phys. Lett. **162**, 455 (1989).
[4] J. R. G. Thorne, S. T. Repinec, S. A. Abrash, J. M. Ziegler, and R. M. Hochstrasser, Chem. Phys. **146**, 315 (1990).
[5] A. Tigler, H. P. Trommsdorf, J. M. Ziegler, and R. M. Hochstrasser, J. Chem. Phys. **96**, 781 (1992).
[6] Z. G. Soos and R. G. Kepler, Phys. Rev. B **43**, 11 908 (1991).
[7] M. Kuwata-Gonokami *et al.*, Nature **367**, 47 (1994).
[8] M. Ueta, H. Kanzaki, K. Kobayashi, Y. Toyozawa, and E. Hanamura, *Excitonic Processes in Solids* (Springer-Verlag, Berlin, 1986).
[9] A. Mysyrowicz, J. B. Grun, R. Levy, A. Bivas, and S. Nikitine, Phys. Lett. **26A**, 615 (1968).
[10] P. C. M. Williams, G. W. Hayden, and Z. G. Soos, Phys. Rev. B **43**, 9777 (1991).
[11] D. Mukhopadhyay, G. W. Hayden, and Z. G. Soos, Phys. Rev. B **51**, 9476 (1995).
[12] Z. G. Soos and G. W. Hayden, Chem. Phys. **143**, 199 (1990).
[13] S. Abe, J. Phys. Soc. Jpn. **58**, 62 (1989).
[14] S. Abe, M. Schreiber, and W. P. Su, Chem. Phys. Lett. **192**, 425 (1992).
[15] V. A. Shakin and S. Abe, Phys. Rev. B **50**, 4306 (1994).
[16] S. Mukamel and H. X. Wang, Phys. Rev. Lett. **69**, 65 (1992).
[17] D. Yaron and R. Silbey, Phys. Rev. B **45**, 11 655 (1992).
[18] F. Guo, M. Chandross, and S. Mazumdar, Phys. Rev. Lett. **74**, 2086 (1995).
[19] H. Tachibana, M. Matsumoto, Y. Tokura, Y. Moritomo, A. Yamaguchi, S. Koshihara, R. D. Miller, and S. Abe, Phys. Rev. B **47**, 4363 (1993).
[20] T. Hasegawa, Y. Iwasa, H. Sunamura, T. Koda, Y. Tokura, H. Tachibana, M. Matsumoto, and S. Abe, Phys. Rev. Lett. **69**, 668 (1992).
[21] F. B. Gallagher and F. C. Spano, Phys. Rev. B **50**, 5370 (1994).
[22] T. Ostreich and K. Schonhammer, Solid State Commun. **85**, 629 (1993).
[23] K. Ishida, J. Phys. Condens. Matter **7**, 3905 (1995).
[24] A. L. Ivanov and H. Haug, Phys. Rev. B **48**, 1490 (1993).
[25] P. N. Butcher and D. Cotter, *The Elements of Nonlinear Optics* (Cambridge University Press, Cambridge, 1990).
[26] F. C. Spano, Chem. Phys. Lett. **234**, 29 (1995); F. C. Spano and E. S. Manas, J. Chem. Phys. **103**, 5939 (1995).
[27] H. Ezaki, T. Tokihiro, and E. Hanamura, Phys. Rev. B **50**, 10 506 (1994).
[28] J. Knoester and F. C. Spano, Phys. Rev. Lett. **74**, 2780 (1995).
[29] H. Bock, W. Ensslin, F. Feher, and R. Freund, J. Am. Chem. Soc. **98**, 668 (1976).
[30] K. Ishida, H. Aoki, and T. Chikyu, Phys. Rev. B **47**, 7594 (1993).